Shock Waves (2026) 36:31
https://doi.org/10.1007/s00193-026-01292-2

ORIGINAL ARTICLE

Shock structures and post-impact jetting in hypervelocity droplet impingement

M. Viqueira-Moreira[1] · A. R. Dworzanczyk[2] · J. D. Langhorn[2] · M. A. Libeau[3] · J. B. Middlebrooks[3] · N. J. Parziale[2] · C. Brehm[1]

Received: 31 January 2026 / Revised: 28 August 2026 / Accepted: 1 September 2026
© The Author(s) 2026

Abstract
The shock dynamics resulting from high-speed droplet impingement on a rigid surface are investigated employing high-resolution schlieren imaging and numerical simulations based on the five-equation model. A key finding is that, in contrast to the common emphasis on jetting-induced dynamics, the long-time shock morphology is governed not by explosive shocks generated during jetting, but rather by the reflection of the droplet's own shock wave off the solid wall. The resulting shock structure is found to be robust across a wide range of densities and breakup states, and its evolution is shown to depend primarily on the impact Mach number. Axisymmetric and 3D simulations both capture the wall-reflected envelope with high fidelity, despite shared limitations in modeling post-impact jetting dynamics. The presented results clarify the physical mechanisms shaping post-impingement shock evolution and highlight the modeling trade-offs involved in capturing jet-driven transients. This paper provides a unique experimental and numerical dataset that can be used as a reference for future studies.

Keywords High-speed droplet impingement · Computational fluid dynamics · Wall-shock reflection

1 Introduction

High-speed droplet impingement on solid surfaces involves complex multiphase interactions in which shock evolution, droplet deformation, and jetting phenomena are coupled nonlinearly. This process is of particular relevance in the context of hypersonic vehicle design, where exposure to rain and particulate environments can lead to significant material degradation. A salient feature of these impacts is the formation of strong shock waves and high-pressure zones generated during the initial compressive interaction between the droplet and the solid substrate.

Foundational studies of high-speed liquid drop impact [1–3] have predominantly focused on the early phase of the impact. These works rigorously analyzed the transient pressure distributions during the initial compression, often using either simplified analytical models or axisymmetric acoustic approximations. Engel et al. [1] systematically characterized the no-flow regime and derived criteria for the onset of radial liquid motion based on pressure wave propagation within the drop. Heymann et al. [2] extended these findings using a quasi-steady compressible formulation, explaining that the maximum pressures occur at the rim just before lateral outflow commences, but still within the first tens of nanoseconds post-impact. Lesser et al. [3] introduced an elegant self-similar geometric-acoustics framework that reinforced these early-time perspectives, albeit with added insight into wavefront curvature and shock attachment limits.

What unites these classical studies is their confinement to the pre-ejection regime, where either analytical tractability or experimental constraints restrict attention to short timescales and radial expansion zones near the contact edge. As a

Communicated by H. Kleine.

This paper is based on work that was presented at the 35th International Symposium on Shock Waves (ISSW35), Brisbane, Australia, July 5–14, 2025.

✉ M. Viqueira-Moreira
manuel.viqueiramoreira@dlr.de

C. Brehm
cbrehm1@umd.edu

[1] Department of Aerospace Engineering, University of Maryland, College Park, MD 20740, USA

[2] Department of Mechanical Engineering, Stevens Institute of Technology, Hoboken, NJ 07030, USA

[3] Integrated Engagement Systems Department, Naval Surface Warfare Center Dahlgren Division, Dahlgren, VA 22448, USA

Published online: 17 October 2026

result, the dynamics beyond this initial phase—especially those governing the formation, evolution, and reflection of shocks in the post-impingement and jetting regime—have remained underexplored. Yet, it is precisely these phenomena that become dominant in practical contexts involving high-Mach-number projectiles, where flow structures persist long after initial impact and can involve repeated shock interactions and complex water jet physics.

In the broader fluid dynamics literature, the long-term physical processes following droplet impingement—such as maximum spreading, splashing, receding, and secondary atomization—have been extensively characterized under low-to-moderate velocity regimes [4, 5]. These classic studies demonstrate how parameters like surface wettability, topological roughness, and liquid viscosity dictate the late-stage lamella development and subsequent rim destabilization or crown formation. Similarly, the macro-mechanics governing aerodynamic droplet breakup (aerobreakup) prior to wall impact have been well-mapped across various Weber number conditions [6]. However, while these conventional long-time descriptions are primarily driven by an interplay of inertial, viscous, and capillary forces, the physics shifts dramatically in hypersonic regimes.

Wu et al. [7] conducted a detailed numerical study of cylindrical droplet impacts at velocities up to 200 m/s, focusing on internal shock formation, rarefaction focusing, and cavitation effects within the liquid phase. This work, performed in 2D axisymmetric geometry, captured the emergence of curved internal shock fronts but did not consider the surrounding gas or any post-ejection dynamics. In a follow-up study, Wu et al. [8] introduced embedded air and vapor cavities into the droplets, analyzing their collapse under compressive shock loading and the resulting internal jetting phenomena—still within a purely numerical and axisymmetric framework. More recently, Wu et al. [9] examined the influence of concave and convex wall geometries on internal shock behavior, showing how substrate curvature modifies wave focusing and cavitation onset. While these three studies offer valuable insights into compressible liquid response, they remain limited by their moderate impact speeds, simplified two-dimensional geometries, and absence of experimental validation. Crucially, they do not simulate the air phase at all. As such, they cannot be considered truly multiphase in nature: without capturing the joint evolution of gas and liquid domains—especially in the post-impact regime where shocks, jets, and ejecta interact across phase boundaries—their approach remains fundamentally single-medium in scope.

Our study addresses this gap by focusing on the temporal evolution of shock structures in the far field after droplet impingement has occurred. Based on recent high-speed visualizations and numerical validation studies [10], we demonstrate that the long-term shock morphology is dictated not by what has been believed to be "explosive shocks" triggered by jetting events, but rather by the trajectory and wall reflection of the droplet's own reflected shock wave. The shock features are robust across a range of impact conditions and are ultimately governed by the projectile Mach number, independent of the fine details of droplet breakup.

The early shock evolution is characterized by two distinct dynamic events. When the droplet retains coherence upon impact, transient shocks generated from high-speed wall jets can reach the wall-reflected shock and momentarily alter the shock structure. However, if the droplet is sufficiently broken up before impingement, the jets lack the coherence and velocity to catch up, and the wall-reflected wave advances cleanly, dominating the flow field. Figure 1 presents numerical schlieren snapshots confirming this behavior: in the less disintegrated case (top), jet-driven shocks visibly interact with the wall-reflected shock; in the more broken-up case (bottom), the primary shock structure remains undisturbed by the weaker jet-induced disturbances. The two sequences of schlieren images establish a clear link between droplet breakup state and shock envelope evolution.

To the best of our knowledge, this is the first systematic investigation into the shock–shock and shock–surface interactions occurring after the primary droplet impingement phase. While prior work has laid essential groundwork in characterizing early-time pressure and damage mechanisms, we extend the analysis into the complex, multi-reflection regime that defines the true long-time shock dynamics of high-speed droplet impacts.

2 Governing equations and modeling approach

The numerical simulations in this study are based on the five-equation model of Allaire [11]. This model describes compressible two-phase flow, assuming mechanical equilibrium between the phases, and has been widely adopted for problems involving shock–interface interactions.

Unless explicitly stated otherwise, all simulations are performed in three dimensions. Cases using the two-dimensional axisymmetric reduction are explicitly identified.

The five-equation model comprises two phase-mass conservation equations ($k = 1, 2$), one mixture momentum conservation law, one mixture total-energy conservation law, and one independent volume-fraction equation, giving $2 + 1 + 1 + 1 = 5$. The vector momentum equation counts as one conservation law. Only one volume fraction is independent because $\alpha_1 + \alpha_2 = 1$. These governing equations are:

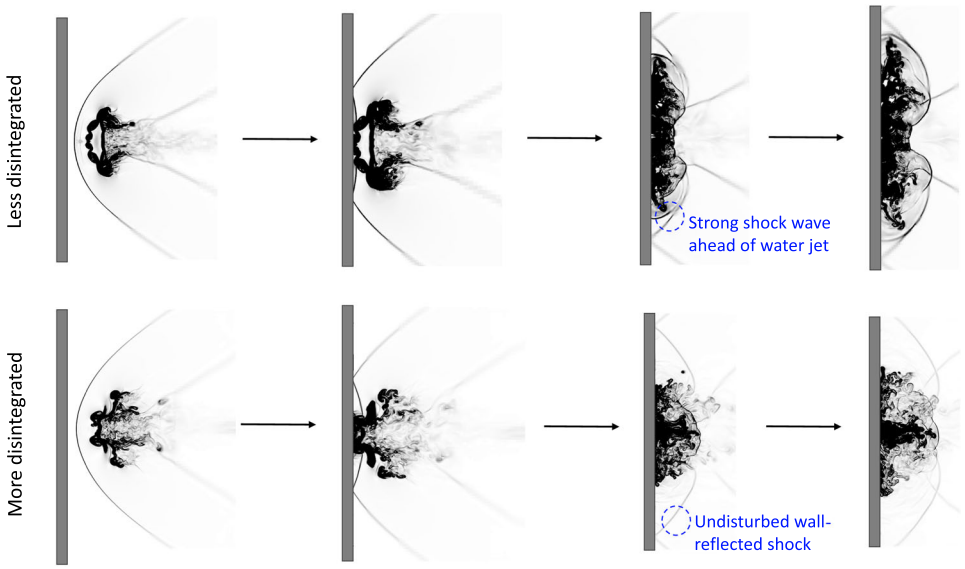

Fig. 1 Numerical schlieren rendering of impact dynamics for a less disintegrated droplet (top), where jet-driven shocks catch up with the main reflected wave, and a more broken-up droplet (bottom), where the wall-reflected shock propagates cleanly ahead and dominates the shock dynamics

1. Conservation of mass (for each phase):

$$\frac{\partial(\alpha_k \rho_k)}{\partial t} + \nabla \cdot (\alpha_k \rho_k \mathbf{u}) = 0, \tag{1}$$

which governs the transport of mass for each phase. Here, α_k is the volume fraction and ρ_k is the density of phase k, where k denotes either the liquid or gas phase; t is time; $\mathbf{u}$ is the common velocity vector; and ∇ is the spatial-gradient operator. The total mixture density is $\rho = \sum_k \alpha_k \rho_k$.

2. Conservation of momentum:

$$\frac{\partial(\rho \mathbf{u})}{\partial t} + \nabla \cdot (\rho \mathbf{u} \otimes \mathbf{u} + p\mathbf{I}) = 0, \tag{2}$$

where p is pressure and $\mathbf{I}$ is the identity tensor.

3. Conservation of total energy:

$$\frac{\partial E}{\partial t} + \nabla \cdot [(E + p)\mathbf{u}] = 0, \tag{3}$$

where $E = \rho e + \frac{1}{2}\rho |\mathbf{u}|^2$ is the total energy density and e is the specific internal energy.

4. Advection of the independent volume fraction α_1:

$$\frac{\partial \alpha_1}{\partial t} + \mathbf{u} \cdot \nabla \alpha_1 = 0. \tag{4}$$

The second volume fraction is given by $\alpha_2 = 1 - \alpha_1$.

To close the system, we employ the stiffened-gas equation of state:

$$p_k = (\gamma_k - 1)\rho_k e_k - \gamma_k p_{\infty,k}, \qquad k = 1, 2, \tag{5}$$

where e_k is the specific internal energy of phase k. Mechanical equilibrium implies $p_1 = p_2 = p$. The equation of state is a closure relation and is not included in the five-equation count. Here, γ_k is the ratio of specific heats and $p_{\infty,k}$ is the stiffened-gas reference pressure for phase k. We use the values from Wong et al. [12]: for liquid water, $\gamma_1 = 6.12$ and $p_{\infty,1} = 3.43 \times 10^8$ Pa; for air, $\gamma_2 = 1.3$ and $p_{\infty,2} = 0$.

Although surface tension and viscous forces influence microscale droplet deformation and atomization in low-speed flows, they can be safely neglected in the present high-speed regime. To justify this omission quantitatively, we estimate the characteristic length scales (r_i) at which these effects become comparable to the dominant inertial forces, following the scaling rationale in Hébert et al. [13]. Capillary forces become relevant when the local Weber number is of order unity, yielding a characteristic radius $r_1 \sim \sigma/(\rho V^2)$, where σ is surface tension and V is the gas velocity. For post-shock gas densities $\rho \in [5.97, 6.53]$ kg/m^3, gas velocities $V \in [1180, 1408]$ m/s, and $\sigma \sim 0.07$ N/m, we find $r_1 \in [5.41, 8.42]$ nm.

Viscous effects become important when the local Reynolds number is of order unity, leading to $r_2 \sim \mu/(\rho V)$, where μ is the liquid dynamic viscosity. Taking $\mu = 1.0 \times 10^{-3}$ kg/(m s) and using the same flow conditions, we obtain $r_2 \in [108.76, 141.95]$ nm. Both r_1 and r_2 are several orders of magnitude smaller than our finest grid spacing $\Delta x = 0.0252$ mm, corresponding to 75 points per droplet diameter, meaning these interfacial features cannot be resolved on a macroscale computational mesh.

Furthermore, the immense dynamic pressures involved at hypersonic speeds completely overwhelm capillary forces. For instance, during a Mach 4.22–4.96 impact, the initial water hammer pressure scales as $P_{\mathrm{wh}} \sim \rho_{\mathrm{l}} c_{\mathrm{l}} V$ and reaches the gigapascal regime ($\sim$ 1.77–2.11 GPa), where ρ_{l} and c_{l} are the liquid density and liquid sound speed, respectively. In contrast, the capillary pressure $P_{\mathrm{c}} \sim 2\sigma/R$, where R is the droplet radius, is only of order 10^2 Pa ($\sim$ 140.70–148.15 Pa) for millimeter-sized droplets with $d_{\mathrm{d}} \in [1.89, 1.99]$ mm; the subscript d denotes droplet. Finally, estimating the thermal-conduction depth via $r_3 \sim (\lambda t_{\mathrm{c}}/\rho_{\mathrm{d}} c_p)^{1/2}$ over the characteristic hydrodynamic timescale $t_{\mathrm{c}} \in [14.4, 20.9]$ µs, where $\lambda = 0.5$ W/m/K is thermal conductivity, $c_p = 4180$ J/kg/K is specific heat at constant pressure, and $\rho_{\mathrm{d}} = 1000$ kg/m^3 is the droplet density, yields $r_3 \in [1.31, 1.58]$ µm, which also remains strictly sub-grid. Because the primary objective of this study is to characterize the far-field macro-shock envelope in the gas phase—which is robustly dictated by the projectile Mach number rather than sub-grid microscale mist physics—excluding surface tension and viscosity is physically justified and computationally necessary.

2.1 Numerical approach

The numerical simulation approach relies on using the positivity-preserving weighted compact nonlinear scheme (WCNS) [12]. This scheme is designed to maintain high-order accuracy in smooth flow regions while resolving shocks and contact discontinuities without spurious oscillations. The compact stencil ensures minimal numerical diffusion, and the nonlinear weighting mechanism adapts to local flow features. Time integration is performed with a third-order strong-stability-preserving Runge–Kutta method. The numerical scheme has been implemented in the CHAMPS solver [14, 15], supporting different immersed boundary method (IBM) schemes [16, 17] and adaptive mesh refinement (AMR).

A key challenge in applying high-order schemes near solid boundaries is the severe reduction of accuracy and potential loss of conservation properties caused by stencil truncation. To overcome this, we implement a specialized *dense boundary condition* (*denseBC*), which substitutes the rigid wall with an artificial, high-density fluid layer. This treatment preserves a sufficiently large acoustic impedance contrast (ρ_{c}) to ensure accurate shock reflection modeling while allowing the full numerical stencil to remain intact. Consequently, the positivity-preserving qualities and robustness of the high-order algorithm are maintained without ad-hoc boundary stencil modifications.

While minor numerical artifacts appear over time in the immediate impact region—such as microscopic filaments of the dense-fluid layer stripping and merging with the liquid phase—the macroscopic shock dynamics remain completely intact. Crucially, the *denseBC* layer acts as an effective, high-inertia "no-slip" boundary that forces the local fluid velocity to zero. During the impact and subsequent jetting phases, the liquid jet velocities are amplified by a factor of 2–3 relative to the already hypersonic projectile velocity (U_{P}, where P denotes projectile). Resolving a true physical viscous boundary layer at these extreme speeds and small scales is computationally intractable.

Capturing this velocity deceleration at the wall is paramount for accurately modeling the macroscale physics. As demonstrated in the Appendix, a standard no-slip wall boundary condition forces the high-speed jet to remain non-physically parallel and attached to the wall—a behavior similar to that of an inviscid slip wall. This artificial attachment subsequently distorts the lateral shock propagation in the gas phase. In contrast, the *denseBC* approach successfully yields the physically expected jet-lifting behavior under reasonable grid resolutions, making it a physically justified and numerically robust surrogate for the solid wall.

2.2 Applicability and limitations of the five-equation model

The five-equation model employed in the present study has demonstrated substantial utility in the simulation of compressible multiphase flows, particularly in aerobreakup scenarios [10]. Owing to its relative simplicity and computational efficiency, this formulation remains a widely adopted numerical approach for resolving shock–drop interactions and the associated deformation processes. However, as shown in prior work [18], this model exhibits significant limitations when applied to flow regimes involving post-impingement jetting dynamics, which emerge following droplet impact.

In particular, the seven-equation model, specifically the dense–dilute formulation, introduces independent evolution equations for phase velocities and energies, thereby enabling a more detailed description of phase separation dynamics. This capability is critical for resolving the hollow jet structures, termed "water arrows" in previous studies, that characterize the post-impingement flow field. These jets were observed to exhibit concentrated liquid mass at their tips, with a well-defined hollow core along their length, and numerous features are entirely absent in the predictions when employing the five-equation system. Instead, the five-equation model yields a much smaller number of jets that are non-hollow, fully water-filled, and significantly diffused at the tip.

The primary source of this discrepancy lies in the inability of the five-equation model to adequately relax negative pressures in regions of intense expansion. In the absence of phase pressure disequilibrium handling, the model artificially sustains tensile stresses inside the jets at stages where water

should have already atomized. The real jets, as observed experimentally, are composed of small, dispersed water particles. In contrast, the seven-equation model incorporates a pressure relaxation treatment that mitigates these nonphysical effects, while enabling treating water as a dispersed phase by default. This allows the formation and evolution of jets whose shapes are qualitatively similar to those observed in experiments.

Nevertheless, despite its superior qualitative performance in modeling post-impingement jetting, the seven-equation model suffers from numerical stability challenges, particularly in the presence of strong shocks and steep interfacial gradients. The pressure relaxation step is not inherently boundedness-preserving with respect to the volume fractions, and under these extreme conditions, the method is prone to numerical failure. These stability issues significantly hinder its robustness in fully capturing the initial shock–drop interaction phase and the subsequent aerobreakup process. For this reason, the present study adopts the five-equation model as the primary tool for investigating the shock-driven deformation and breakup dynamics, as well as late-stage shock structures, while recognizing its inherent limitations in describing the post-impingement jetting behavior.

Crucially, the nature and internal structure of the jets influence their localized, transient dynamics. The hollow, low-inertia jets predicted by a seven-equation model eject at higher initial velocities but decelerate rapidly. Conversely, the dense, fully water-filled jets generated by the five-equation model eject at lower initial speeds but maintain their momentum over longer distances due to their higher localized inertia. However, by fundamental principles of momentum conservation, the integrated kinetic energy transferred from the droplet to the surrounding gas phase remains invariant. Because the high-speed liquid phase acts as an aerodynamic piston driving the gas regardless of its internal phase distribution, the outer gas-phase shocks are observed to converge onto common, identical trajectories within less than 5 μs following impact.

To ensure a balanced interpretation of the narrative, the findings presented herein must therefore be demarcated into two distinct categories of modeling reliability:

1. **Quantitatively reliable features:** The gas-phase macro-shock envelope trajectories (both normal and lateral shocks), macro-shock propagation velocities, and the peak substrate impact pressures prior to ejection. Driven by global conservation laws and gas-phase aerodynamics, these macro-features are robustly captured and remain insensitive to sub-grid liquid morphology.
2. **Qualitative/illustrative features:** The fine-scale internal morphology of the liquid jets (solid vs. hollow cores), the exact number of localized micro-jets, and late-stage liquid mist atomization patterns.

Consequently, while the five-equation model provides an exceptionally robust and quantitatively reliable framework for mapping the macroscale shock structures investigated in this study, fine-scale conclusions regarding liquid jet topologies must be interpreted as qualitative indicators of the underlying momentum exchange.

3 Simulation setup

To study the post-breakup shock dynamics resulting from high-speed droplet impingement, we adopt a numerically tractable approach that isolates the essential gas–liquid interaction while avoiding the complexity of simulating the full projectile geometry. The initial breakup phase is modeled as a canonical shock–droplet interaction, in which a planar shock propagates toward and interacts with a stationary droplet. Comparison with full-domain simulations that retain the projectile throughout confirms the validity of this approach. After a time corresponding to the experimentally measured interval between shock impact and droplet–wall contact, the simulation is reinitialized in a disintegrated post-shock configuration. The entire computational domain is then Galilean-transformed so that the post-shock gas becomes stationary, and a static wall is introduced to emulate the impingement surface. Further details on the dense-fluid boundary condition are provided in the Appendix.

To minimize artificial boundary reflections and ensure numerical robustness, the Galilean transformation is performed using the post-shock gas velocity u_2, i.e., the gas velocity behind the incident shock in the laboratory frame. This differs from a transformation into the pure projectile-fixed frame (which would adopt U_P), but it preserves well-posedness at the domain boundaries and eliminates spurious back-pressure buildup at the newly introduced wall. While this approach introduces a slight discrepancy with respect to the experimental frame of reference, it enables a clean and repeatable numerical setup that isolates the essential shock–droplet physics without introducing numerical artifacts. Importantly, the transformation maintains the correct relative velocity between the shock and the droplet, thus preserving the fidelity of the interaction dynamics.

A schematic of the simulation domain and mesh layout is shown in Fig. 2a, b, illustrating the shock orientation, droplet initialization, and transformed flow direction. To facilitate direct comparison with experiments, two representative cases are simulated: **drop 1**, corresponding to a more disintegrated, lower-Mach-number condition in the test matrix, and **drop 4**, representing a higher-speed, more energetic impact. The key operational and thermodynamic parameters for each case are summarized in Table 1. Here, ρ_1 and ρ_2 denote the ambient pre-shock and post-shock gas densities, respectively; U_P and M_P represent the projectile velocity and Mach number; d_d

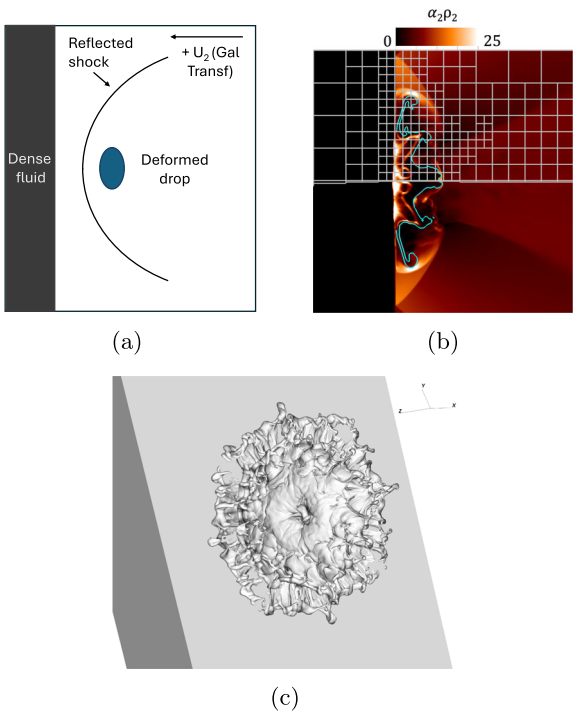

Fig. 2 **a** Simulation setup, **b** planar view of flow and mesh, and **c** 3D post-impingement 10% water volume contour

is the initial droplet diameter; and u_2 is the induced post-shock gas velocity. The primary kinematics (U_P, M_P, and d_d) are taken directly from the experimental shot conditions reported in Dworzanczyk et al. [10], whereas the post-shock gas states (ρ_2, u_2) are analytically computed via standard one-dimensional normal shock relations. Also listed is the time to impact (t_I), which quantifies the exact time elapsed between the initial shock-droplet encounter and physical wall contact, serving as the temporal initialization point for the subsequent impingement phase; the subscript I denotes impact. Details about the experimental configurations can be found in Dworzanczyk et al. [10].

All simulations used for experimental comparison were conducted using AMR, with the finest level corresponding to a uniform resolution of 75 points per droplet diameter (ppd). While our previous aerobreakup [10] studies employed higher resolutions (150 ppd) to resolve small-scale surface instabilities and detailed mass-loss mechanisms, such fidelity is not required here. The present work focuses on the global shock dynamics following impingement, which are well resolved at 75 ppd when combined with the high-order WCNS. An axisymmetric grid-convergence study, shown in the Appendix, confirms that this resolution is sufficient to accurately capture the dominant flow features of interest.

We emphasize that, although the current simulations employ some simplifications—most notably the use of a Galilean transformation rather than resolving the full projectile–droplet interaction—they represent a significant advancement over previous numerical studies of high-speed droplet impact. For example, Tretola and Vogiatzaki [19] simulated droplet impacts up to 500 m/s using a wedge-domain compressible volume-of-fluid (VoF) framework, but employed a simplified axisymmetric geometry with imposed symmetry and no post-impact shock evolution. Their analysis focused on internal compression waves and lamella formation on a solid wall, without resolving jet dynamics, reflected shocks, or realistic shock–droplet interactions. In contrast, the present setup explicitly captures both the initial and wall-reflected shocks, along with the transient, jet-driven flow features that characterize physically realistic impingement scenarios. A snapshot in Fig. 2c shows the three-dimensional post-impingement state for drop 4, visualized using water-volume-fraction contours. By matching pre-impingement states to experimental measurements, the model retains physical fidelity while avoiding the initialization errors and interfacial noise seen in prior work.

4 Results and discussion

4.1 Comparison of the evolution of the shock envelope

The evolution of the shock envelope following droplet impingement is assessed through comparison between experimental schlieren imaging and numerical simulations. Figure 3 presents time-resolved schlieren images from high-speed experiments, spanning $t = 2$–7 μs for two representative cases—drop 1 and drop 4. In the early stages, the shock structure is influenced by transient shocks generated during the jetting phase. At later times, the flow is dominated by the outward propagation of the wall-reflected shock, which defines the long-time morphology of the envelope.

To compare simulations against these measurements, we extract the shock envelope from both three-dimensional and axisymmetric simulations and overlay them with experimental data, as shown in Fig. 4. These comparisons reveal strong

Table 1 Shot conditions used in simulation cases

Drop	ρ_1 (kg/m^3)	ρ_2 (kg/m^3)	U_P (m/s)	M_P	d_d (mm)	u_2 (m/s)	t_I (μs)
1	1.18	5.97	1469	4.22	1.89	1180	20.9
4	1.18	6.53	1717	4.96	1.99	1408	14.4

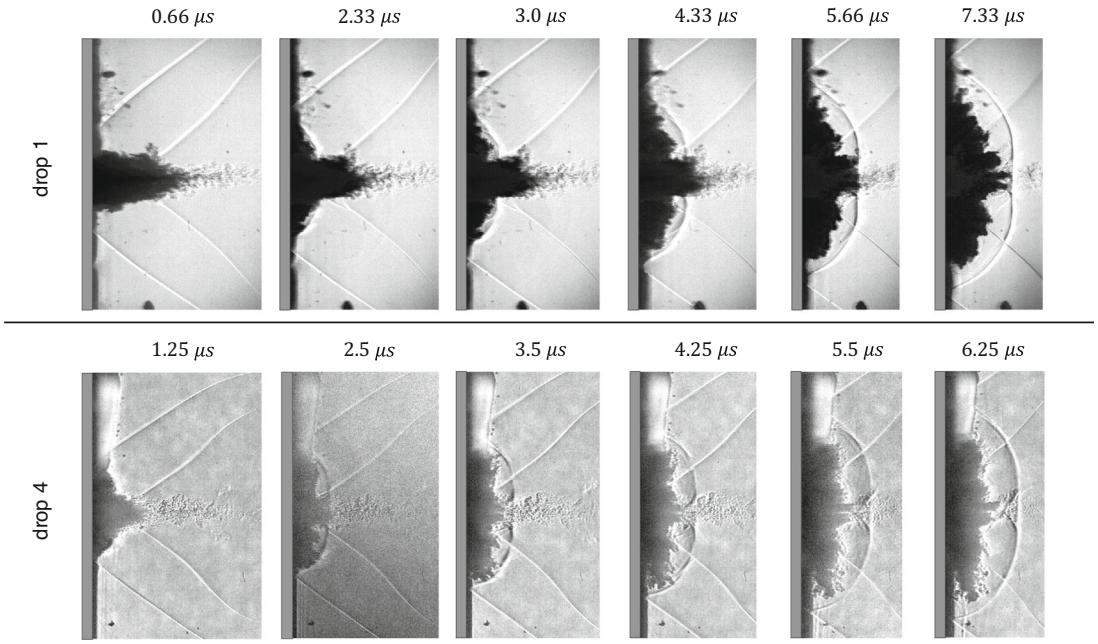

Fig. 3 Schlieren images with time measured from the moment of wall impact

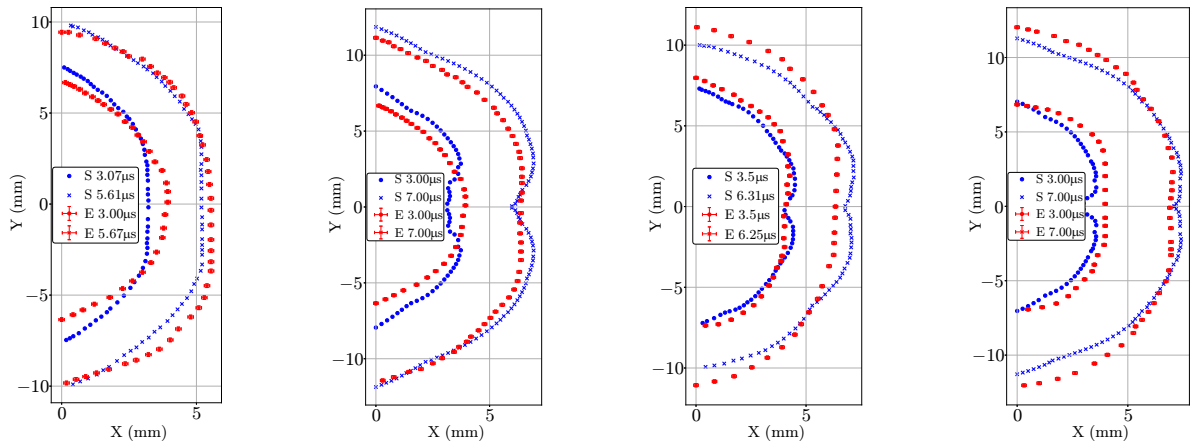

Fig. 4 Comparison of experimental (E) and numerical (S) shock envelopes for drops 1 (**a**, **b**) and 4 (**c**, **d**)

agreement across both cases, with the numerical shock fronts closely tracking the experimental envelope throughout the simulation window. For drop 1, where the droplet is more disintegrated prior to impact, jetting is weaker and plays a limited role in shaping the envelope. The shock dynamics are governed almost entirely by the wall-reflected structure, and both axisymmetric and three-dimensional simulations reproduce the envelope with high fidelity. This is consistent with findings by Hebert et al. [13], Viqueira-Moreira et al. [20], who showed that the reflected shock structure generated by a disintegrated droplet can be captured accurately using axisymmetric approaches. For drop 4, which features a less disintegrated droplet and higher impact momentum, the initial pressure pulse and associated jet-driven shocks are stronger. While these effects briefly influence the envelope at early times, they decay rapidly, and the dominant shock structure again becomes the wall-reflected shock. As with drop 1, both simulation approaches yield comparable results, with only minor deviations from the experimental envelope.

Complementary schlieren cut-plane renderings from the three-dimensional simulations are provided in Fig. 5. These snapshots capture the temporal evolution of the shock field, from initial impact through the formation of the late-time, outward-propagating wall-reflected shock.

For drop 1, a persistent spurious structure is visible throughout the entire time sequence, marked by a red

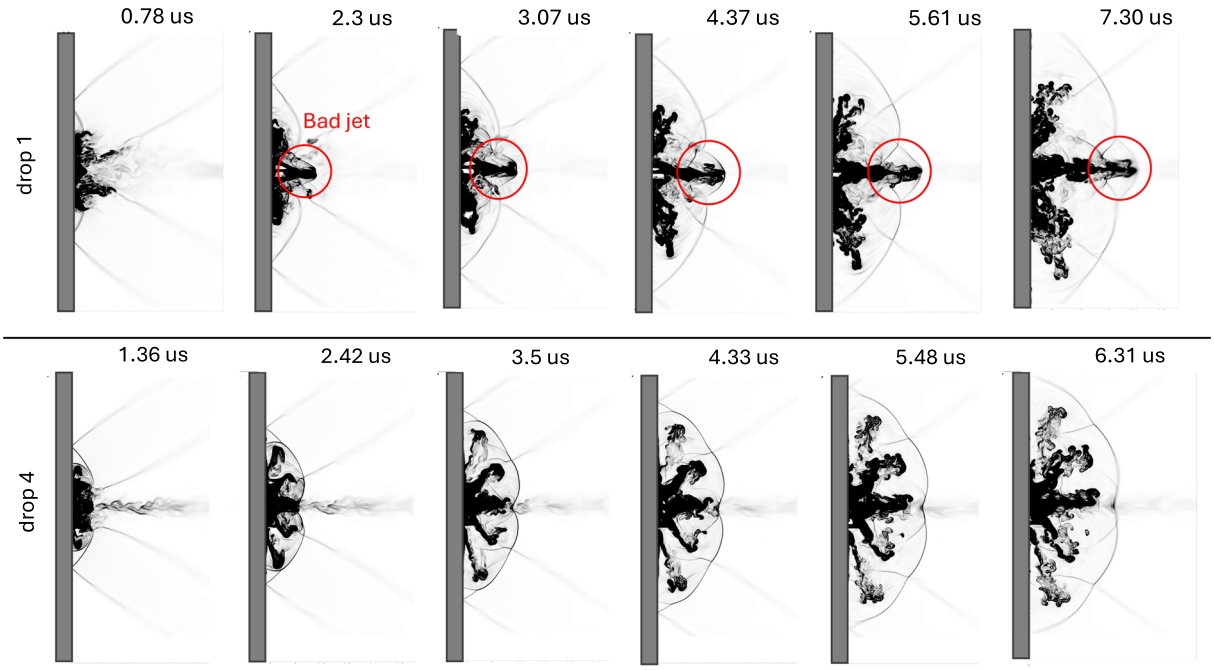

Fig. 5 Numerical schlieren images for drops 1 and 4. Time is measured from the moment of wall impact

circle in the figure. This feature—referred to here as a "bad jet"—is a numerical artifact arising from the limitations of the five-equation model, which does not adequately capture post-impingement jetting dynamics. The resulting jet-like structure is overly coherent and unphysical, differing significantly from experimentally observed behavior. To ensure the fidelity of the quantitative comparison, this region is excluded from all shock envelope extractions and normal shock position tracking for drop 1.

The tracked positions of the normal and lateral shocks are shown in Fig. 6a, b, comparing simulation results with experimental measurements. Close agreement is found in both directions, particularly for drop 1, where the shock field is dominated by the wall-reflected structure and remains largely unaffected by the spurious jet. Overall, these results highlight that, for the shock envelope associated with post-impingement wall reflections, three-dimensional and axisymmetric models perform similarly, and both are capable of reproducing experimental observations with high accuracy—even when using a simplified five-equation formulation.

4.2 Influence of droplet material on shock structure

To isolate how droplet density and compressibility influence the resulting shock dynamics, simulations were performed across a wide parametric sweep of four materials: methanol (0.787 g/cm^3), water (1.0 g/cm^3), "fake aluminum" (2.7 g/cm^3), and gallium (6.1 g/cm^3). These fluids

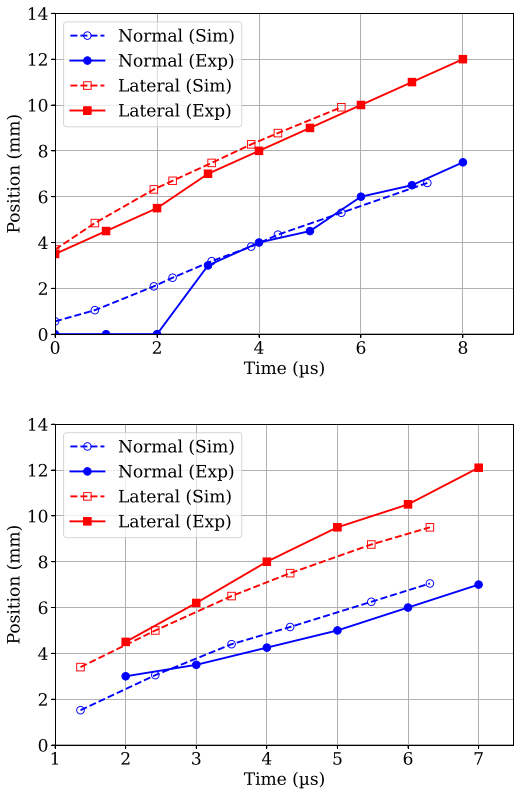

Fig. 6 Experimental and numerical shock positions for drops 1 (**a**) and 4 (**b**)

were modeled using a stiffened-gas equation of state (SG-EOS) to provide a broad range of ambient densities and internal acoustic impedances ($Z_l = \rho_l c_l$, where Z_l is the liq-

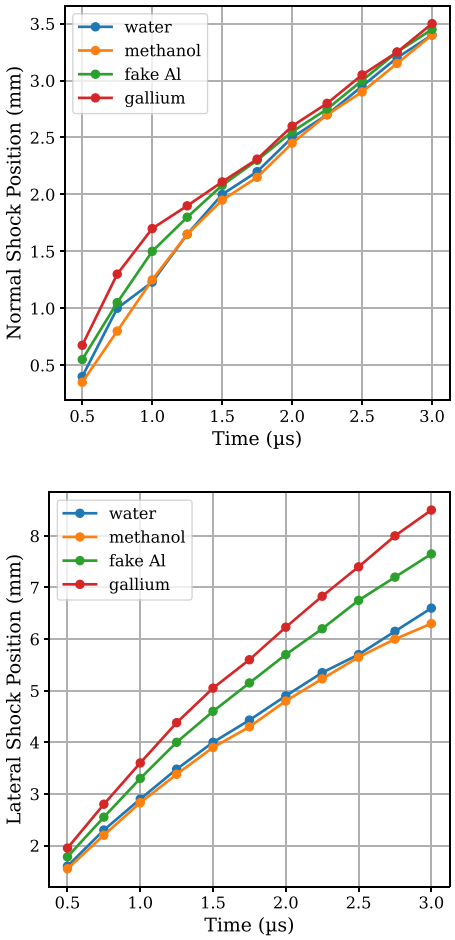

Fig. 7 Normal (**a**) and lateral (**b**) shock positions for droplets of different densities

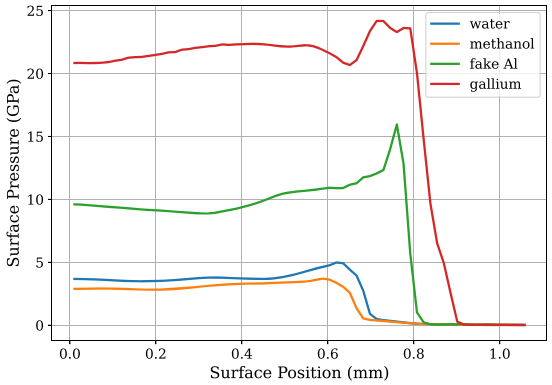

Fig. 8 Surface pressure distribution just prior to jet ejection. Higher-density liquids exert larger impact pressures

uid acoustic impedance). The "fake aluminum" configuration adopts the properties of liquid aluminum at ambient temperature to serve as a high-density, stiff proxy—allowing us to isolate heavy material impacts without introducing complex, temperature-dependent phase changes. For all comparative cases, the AMR resolution was held strictly constant at 140 points per droplet diameter (ppd).

Figure 7a, b plots the temporal evolution of the normal and lateral shock positions across the material matrix. A profound physical decoupling is observed in the normal shock trajectory (Fig. 7a): Despite the massive discrepancies in liquid density, internal speed of sound, and acoustic impedance among the four fluids, all trajectories converge seamlessly onto a common path beyond $t \gtrsim 2$ μs. This convergence robustly demonstrates that the normal component of the macro-shock envelope becomes completely independent of the internal droplet material or its specific EOS parameters after the initial transient splash. Because the normal shock is a gas-phase wave propagating vertically away from the substrate, the flattened droplet residue acts merely as a passive geometric boundary, preventing any further mechanical energy transfer from the liquid phase into the normal direction. Instead, its late-time evolution is exclusively dictated by gas-phase shock reflection and the surrounding aerodynamics.

Conversely, the lateral shock propagation (Fig. 7b) remains strongly coupled to the specific fluid material properties during the early stages ($t < 3$ μs) due to an active, jet-driven mechanism. Denser and stiffer liquids possess a significantly higher acoustic impedance, which restricts internal droplet compressibility and drastically elevates the initial impact footprint. As corroborated by the surface pressure profiles just prior to jet ejection in Fig. 8, liquids with higher densities and stiffnesses—most notably fake Al and gallium—generate highly elevated wall pressures. These extreme localized pressures drive intensely vigorous lateral liquid jetting almost parallel to the substrate. Because these high-speed jets act as active aerodynamic pistons pushing into the surrounding gas, the resulting lateral blast waves exhibit sharper, more rapidly expanding fronts that are clearly stratified by the material properties.

Ultimately, this comparative material study reveals that while the internal fluid properties and liquid speed of sound heavily influence the transient, early-time localized jetting shocks, they exert virtually no influence on the long-term far-field macro-shock scenario, which remains a robust feature of gas-phase dynamics. To definitively substantiate this decoupling and isolate the pure gas-phase mechanics from any lingering liquid jet interactions, a targeted numerical experiment is presented in the following section wherein the droplet is artificially removed from the computational domain immediately after the impact transient.

4.3 Disentangling jet-driven and wall-reflected shocks by artificial droplet removal

Simulated shock envelopes for drops 1 and 4 are presented in Fig. 9, comparing cases with and without the droplet present at the time of impact. In the "without drop" scenario, the

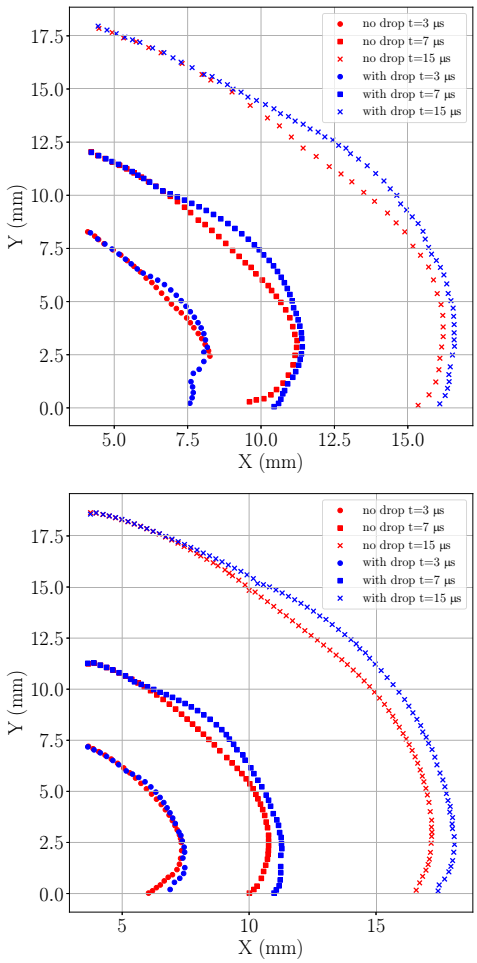

Fig. 9 Shock envelopes at different times post-impact for two representative axisymmetric shots: **a** drop 1 and **b** drop 4. Red symbols represent runs in which the droplets have been artificially removed prior to impingement

droplet is artificially removed just prior to wall interaction and replaced with air at the reflected shock conditions. It must be emphasized that this non-physically realizable flow configuration serves strictly as an idealized diagnostic numerical test rather than a predictive model. Its sole utility lies in isolating the standalone geometric contribution of the wall-reflected wave from the concurrent liquid dynamics.

The "with drop" cases exhibit additional transient features arising from jetting, but these disturbances are short-lived. Despite their early influence, jet-driven shocks do not substantially alter the final shape of the shock envelope, which is ultimately governed by the dominant wall-reflected structure. This diagnostic test robustly confirms that jet-induced shocks, while visually striking, may be safely neglected in reduced-order models aimed at capturing the late-time shock morphology.

5 Conclusion

This study provides a comprehensive examination of shock evolution in high-speed droplet impingement, with emphasis on distinguishing the contributions of jet-driven and wall-reflected shock structures. Through direct comparison with high-speed schlieren imaging, we show that the long-time morphology of the shock envelope is dominated by the wall-reflected component, while transient jet-induced shocks decay rapidly and exert minimal influence on the overall flow.

Our findings demonstrate that this dominant wall-reflected structure is largely insensitive to the degree of droplet disintegration and instead scales primarily with the impact Mach number. This insight explains the close agreement of axisymmetric simulations in predicting the envelope evolution, even in scenarios where three-dimensional jetting is expected. A dedicated numerical experiment confirms that removing the droplet altogether has only a minor effect on the final shock envelope, further reinforcing the secondary role of jet-induced structures.

These results clarify the physics of shock–surface interactions following droplet impact and establish a framework for future modeling efforts. Accurate prediction of post-impingement shock morphology does not necessarily require full three-dimensional jet resolution; instead, it depends on capturing the dominant wall-reflected wave, which can be achieved with axisymmetric simulations under appropriate boundary treatment. Future work will target improved jet modeling using higher-fidelity multiphase formulations, such as the seven-equation model, to address remaining limitations in explosive water jet structure.

Appendix

Boundary conditions and numerical implementation

In the present simulations, a high-order WCNS was used to resolve the compressible multiphase flow dynamics. Traditional no-slip boundary conditions, although physically appropriate for solid walls, compromise the high-order accuracy of WCNS discretizations near boundaries due to stencil truncation effects and are prone to numerical instabilities in extreme scenarios such as high-Mach-number droplet impingement. To address this issue, a modified boundary treatment referred to as the *denseBC* was employed.

The *denseBC* introduces a high-density fluid layer ($\sim 1 \times 10^6$ g/cm^3) inside the computational boundary. Rather than explicitly enforcing zero velocity at the wall, the boundary condition relies on the large impedance mismatch between the physical fluid and the dense ghost layer to strongly suppress normal velocity components and to reflect acoustic waves. In addition, momentum conservation across

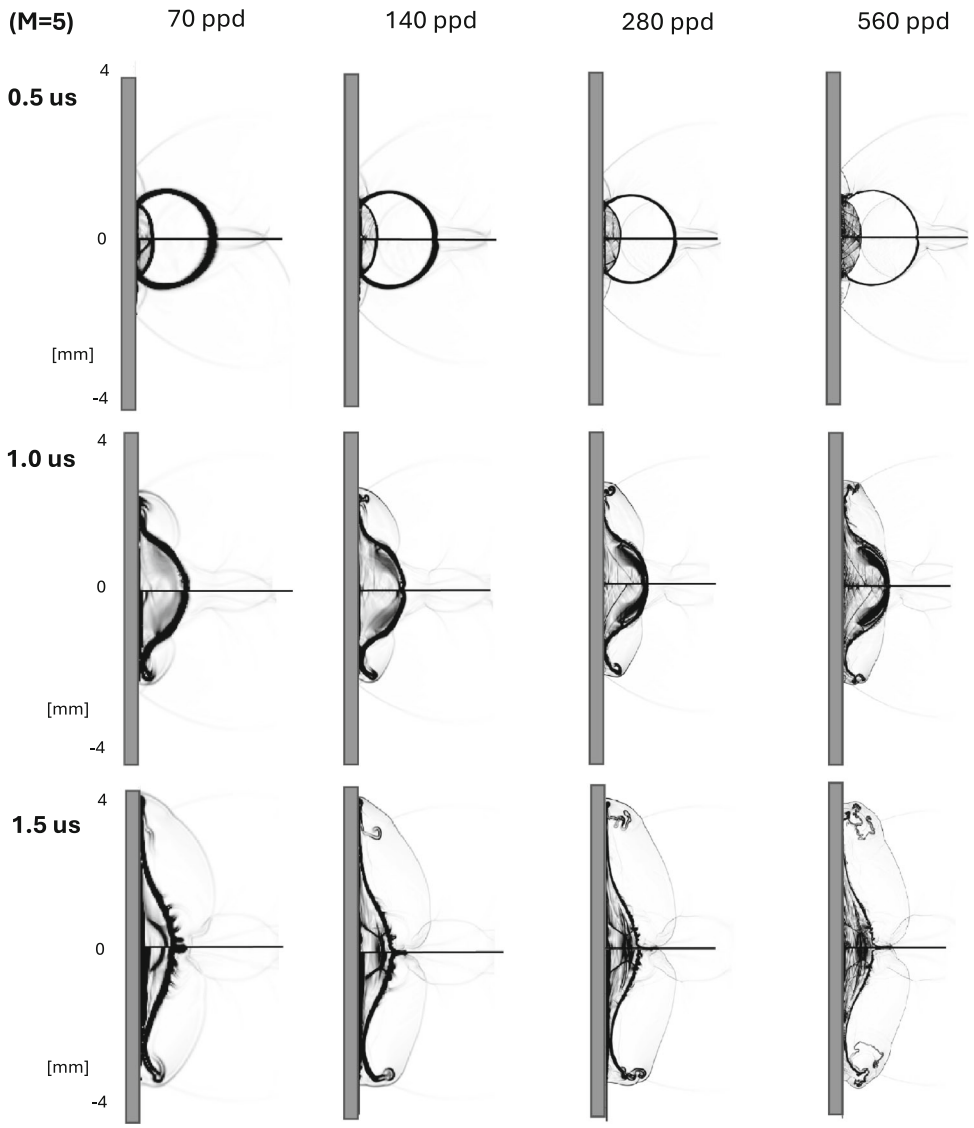

Fig. 10 Comparison of post-impact jet formation between MUSCL + THINC with no-slip boundary conditions (upper-side) and WCNS with the *denseBC* approach (lower-side), across simulations with 4, 5, 6, and 7 AMR levels

the interface ensures that the effective momentum exchange with the dense layer leads to near-zero wall velocities, such that the boundary behaves, to leading order, as a no-slip wall.

The purpose of this appendix is not to advocate *denseBC* as a physical wall model, but as a numerically consistent boundary treatment that preserves high-order accuracy and stability.

A comparison between a lower-order MUSCL+THINC scheme using classical no-slip conditions and the present WCNS+*denseBC* approach is shown in Fig. 10. Despite the robustness of the MUSCL+THINC method and its ability to maintain sharp interfaces, it consistently fails to reproduce the initial vertical jet lift observed experimentally. Instead, the jet remains confined along the wall, leading to a spurious lateral flow and the formation of nonphysical surface-parallel jets. These features severely disrupt the shock structure by creating elongated, wall-attached shocks that are inconsistent with both analytical expectations and high-speed imagery.

The WCNS method combined with the *denseBC* treatment, on the other hand, successfully captures the vertical lift of the jet even with fewer AMR levels. This correct deflection of the jet is critical in allowing the system to relax pressure appropriately and to avoid artificial confinement effects near the wall. Furthermore, the improved fidelity in capturing jet lift directly impacts the evolution of lateral shocks, yielding a more accurate description of shock propagation and convergence.

These results confirm the necessity of matching high-order spatial schemes with compatible boundary strategies. For simulations aiming to replicate realistic post-impact dynamics, the *denseBC* boundary is a valuable tool for preserving both numerical stability and physical accuracy.

Funding Brehm and Viqueira-Moreira were supported by ONR Grant N00014-22-1-2443. Eric Marineau of Code 351 is the Program Officer for both grants. Dworzanczyk, Langhorn, and Parziale were supported by ONR-MURI Grant N00014-20-1-2682.

Data availability The simulation outputs used in this study are available from the corresponding author upon reasonable request.

Code availability The CHAMPS solver is not publicly released. Relevant configuration files or portions of the code are available from the authors upon reasonable request.

Declarations

Conflict of interest The authors declare that they have no conflict of interest.

Open Access This article is licensed under a Creative Commons Attribution 4.0 International License, which permits use, sharing, adaptation, distribution and reproduction in any medium or format, as long as you give appropriate credit to the original author(s) and the source, provide a link to the Creative Commons licence, and indicate if changes were made. The images or other third party material in this article are included in the article's Creative Commons licence, unless indicated otherwise in a credit line to the material. If material is not included in the article's Creative Commons licence and your intended use is not permitted by statutory regulation or exceeds the permitted use, you will need to obtain permission directly from the copyright holder. To view a copy of this licence, visit http://creativecommons.org/licenses/by/4.0/.

References

1. Engel, O.G.: Damage produced by high-speed liquid-drop impacts. J. Appl. Phys. **44**, 692–704 (1973). https://doi.org/10.1063/1.1662246
2. Heymann, F.J.: High-speed impact between a liquid drop and a solid surface. J. Appl. Phys. **40**, 5113–5122 (1969). https://doi.org/10.1063/1.1657361
3. Lesser, M.B., Field, J.E.: The impact of compressible liquids. Annu. Rev. Fluid Mech. **15**, 97–122 (1983). https://doi.org/10.1146/annurev.fl.15.010183.000525
4. Yarin, A.L.: Drop impact dynamics: splashing, spreading, receding, bouncing... Annu. Rev. Fluid Mech. **38**, 159–192 (2006). https://doi.org/10.1146/annurev.fluid.38.050304.092144
5. Josserand, C., Thoroddsen, S.: Drop impact on a solid surface. Annu. Rev. Fluid Mech. **48**, 365–391 (2016). https://doi.org/10.1146/annurev-fluid-122414-034401
6. Guildenbecher, D.R., López-Rivera, C., Sojka, P.E.: Secondary atomization. Exp. Fluids **46**, 371–402 (2009). https://doi.org/10.1007/s00348-008-0593-2
7. Wu, W., Xiang, G., Wang, B.: On high-speed impingement of cylindrical droplets upon solid wall considering cavitation effects. J. Fluid Mech. **857**, 851–877 (2018). https://doi.org/10.1017/jfm.2018.753
8. Wu, W., Wang, B., Liu, Q.: Impingement of high-speed cylindrical droplets embedded with an air/vapour cavity on a rigid wall: numerical analysis. J. Fluid Mech. **864**, 1058–1087 (2019). https://doi.org/10.1017/jfm.2019.55
9. Wu, W., Wang, B., Xiang, G.: Curved surface effect on high-speed droplet impingement. J. Fluid Mech. **909**, A7 (2021). https://doi.org/10.1017/jfm.2020.926
10. Dworzanczyk, A.R., Viqueira-Moreira, M., Langhorn, J.D., Libeau, M.A., Brehm, C., Parziale, N.J.: On aerobreakup in the stagnation region of high-Mach-number flow over a bluff body. J. Fluid Mech. **1002**, A1 (2024). https://doi.org/10.1017/jfm.2024.1092
11. Allaire, G., Clerc, S., Kokh, S.: A five-equation model for the simulation of interfaces between compressible fluids. J. Comput. Phys. **181**, 577–616 (2002). https://doi.org/10.1006/jcph.2002.7143
12. Wong, M.L., Angel, J.B., Barad, M.F., Kiris, C.C.: A positivity-preserving high-order weighted compact nonlinear scheme for compressible gas–liquid flows. J. Comput. Phys. **444**, 110569 (2021). https://doi.org/10.1016/j.jcp.2021.110569
13. Hébert, D., Rullier, J.-L., Chevalier, J.-M., Bertron, I., Lescoute, E., Virot, F., El-Rabii, H.: Investigation of mechanisms leading to water drop breakup at Mach 4.4 and Weber numbers above 10^5. SN Appl. Sci. **2**, 69 (2020). https://doi.org/10.1007/s42452-019-1843-z
14. Boustani, J., Barad, M.F., Kiris, C.C., Brehm, C.: An immersed boundary fluid–structure interaction method for thin, highly compliant shell structures. J. Comput. Phys. **438**, 110369 (2021). https://doi.org/10.1016/j.jcp.2021.110369
15. McQuaid, J.A., Brehm, C.: Heat flux predictions for hypersonic flows with an overset near body solver on an adaptive block-structured cartesian off-body grid. Comput. Fluids **269**, 106121 (2024). https://doi.org/10.1016/j.compfluid.2023.106121
16. Brehm, C., Fasel, H.F.: A novel concept for the design of immersed interface methods. J. Comput. Phys. **242**, 234–267 (2013). https://doi.org/10.1016/j.jcp.2013.01.027
17. Brehm, C., Hader, C., Fasel, H.F.: A locally stabilized immersed boundary method for the compressible Navier–Stokes equations. J. Comput. Phys. **295**, 475–504 (2015). https://doi.org/10.1016/j.jcp.2015.04.023
18. Viqueira-Moreira, M., Brehm, C.: Implementation and validation of a 7-equation model for high-speed droplet impingement. AIAA AVIATION Forum, Las Vegas, NV, AIAA Paper 2024-3747 (2024). https://doi.org/10.2514/6.2024-3747
19. Tretola, G., Vogiatzaki, K.: Unveiling the dynamics of ultra high velocity droplet impact on solid surfaces. Sci. Rep. **12**, 7416 (2022). https://doi.org/10.1038/s41598-022-11188-7
20. Viqueira-Moreira, M., Dworzanczyk, A., Parziale, N.J., Brehm, C.: Numerical investigation of droplet aerobreakup and impingement experiments at Mach 5. AIAA AVIATION Forum, San Diego, CA, AIAA Paper 2023-4251 (2023). https://doi.org/10.2514/6.2023-4251

Publisher's Note Springer Nature remains neutral with regard to jurisdictional claims in published maps and institutional affiliations.